

# Directed Urea-to-Nitrite Electrooxidation via Tuning Intermediate Adsorption on Co, Ge Co-Doped Ni Sites

Pengtang Wang, Xiaowan Bai, Huanyu Jin, Xintong Gao, Kenneth Davey, Yao Zheng, Yan Jiao, and Shi-Zhang Qiao\*

The electrochemical urea oxidation reaction (UOR) is an alternative to electrooxidation of water for energy-saving hydrogen ( $H_2$ ) production. To maximize this purpose, design of catalysts for selective urea-to-nitrite ( $NO_2^-$ ) electrooxidation with increased electron transfer and high current is practically important. Herein, a cobalt, germanium (Co, Ge) co-doped nickel (Ni) oxyhydroxide catalyst is reported first time that directs urea-to- $NO_2^-$  conversion with a significant Faradaic efficiency of 84.9% at 1.4 V versus reversible hydrogen electrode and significantly boosts UOR activity to  $448.0 \text{ mA cm}^{-2}$ . Importantly, this performance is greater than for most reported Ni-based catalysts. Based on judiciously combined synchrotron-based measurement, in situ spectroscopy and density functional theoretical computation, significantly boosted urea-to- $NO_2^-$  production results from Co, Ge co-doping is demonstrated that optimizes electronic structure of Ni sites in which urea adsorption is altered as NO-terminal configuration to facilitate C–N cleavage for  $*NH$  formation, and thereby expedites pathway for urea to  $NO_2^-$  conversion. Findings highlight the importance of tuning intermediate adsorption behavior for design of high-performance UOR electrocatalysts, and will be of practical benefit to a range of researchers and manufacturers in replacing conventional water electrooxidation with UOR for energy-saving  $H_2$  production.

For electrocatalytic urea oxidation reaction (UOR), urea is oxidized to N-containing products including, nitrogen ( $N_2$ ), nitrite ( $NO_2^-$ ) and nitrate ( $NO_3^-$ ) under the effect of electrocatalysts together with electron transfer and carbon dioxide ( $CO_2$ ) generation.<sup>[6–8]</sup> Nickel (Ni) and its derivatives are the widely reported as “efficient” catalysts for UOR in alkaline.<sup>[9–21]</sup> Because of the co-effect of alkaline environment and oxidation potential, the surface Ni component on these Ni-based materials will evolve into Ni oxyhydroxide (NiOOH) via a self-oxidation.<sup>[22–27]</sup> These generated NiOOH serve as active sites to react with urea and degrade it through spontaneous redox.<sup>[8,22–24]</sup> Based on this, significant research has focussed on the design and “tailoring” of the structure of Ni-based catalysts with more available NiOOH for enhanced UOR.<sup>[9,24,25]</sup> For example, Chen and co-authors reported that cobalt (Co) doping alters electron density distribution of Ni hydroxide ( $Ni(OH)_2$ ) to decrease the energy barrier for hydrogen defect formation on  $Co_{0.1}Ni_{0.9}(OH)_2$ , leading therefore to a lower generation potential


for NiOOH and boosted UOR activity.<sup>[8]</sup> In addition, through electrochemical leaching of tungstate species from pseudo-crystalline  $NiWO_4$ -TA, Lin and co-authors reported synthesis of a unique NiOOH layer with sufficient dynamic  $Ni^{3+}$  active sites and interphase ion transport to exhibit boosted UOR.<sup>[24]</sup> Despite progress however with Ni-based catalysts for UOR, most reported findings are limited to urea-to- $N_2$  for enhanced UOR.<sup>[12–21]</sup> Products selectivity and possible other reaction pathways for UOR that are responsible for increasing performance are not widely reported.

Compared with urea-to- $N_2$ , electrooxidation urea to over-oxidized products, e.g.,  $NO_2^-$  is more chemically economic for coupling with cathodic  $H_2$  evolution reaction (HER) to produce  $H_2$  (Figure 1). This is because one urea molecule can be only electrochemically oxidized into one molecule  $N_2$  under six electrons transfer. However, once be over-oxidized, it can generate two  $NO_2^-$  with 12 electrons transferred.<sup>[6,23]</sup> The greater the number of transferred electrons on the anode the greater the current when consuming the same amount of urea. In this way, more electric energy will contribute to coupling with cathodic HER for  $H_2$  production. In contrast to the low-valuable and

## 1. Introduction

Electrooxidation of urea from industrial wastewater and urine has received increasing research attention because of ready accessibility, good compatibility and low thermodynamic barrier and, is seen as a practical alternative of oxygen evolution reaction (OER) for energy-saving hydrogen ( $H_2$ ) production.<sup>[1–5]</sup>

P. Wang, X. Bai, H. Jin, X. Gao, K. Davey, Y. Zheng, Y. Jiao, S.-Z. Qiao  
School of Chemical Engineering and Advanced Materials  
The University of Adelaide  
Adelaide, SA 5005, Australia  
E-mail: s.qiao@adelaide.edu.au

 The ORCID identification number(s) for the author(s) of this article can be found under <https://doi.org/10.1002/adfm.202300687>.

© 2023 The Authors. Advanced Functional Materials published by Wiley-VCH GmbH. This is an open access article under the terms of the Creative Commons Attribution License, which permits use, distribution and reproduction in any medium, provided the original work is properly cited.

DOI: 10.1002/adfm.202300687

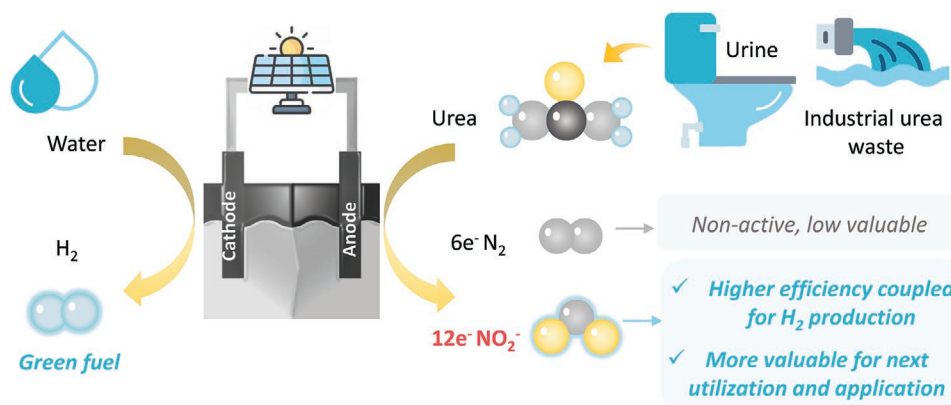


**Figure 1.** Schematic for urea electrooxidation to  $\text{N}_2$  and  $\text{NO}_2^-$ . UOR coupling with HER to generate  $\text{H}_2$  and  $\text{NO}_2^-$  together with practical value for further utilization.

non-activity of  $\text{N}_2$ ,  $\text{NO}_2^-$  is much more readily utilized and transformed to second products with economic value.<sup>[28–33]</sup> Recent studies have reported that  $\text{NO}_2^-$  can be integrated with cyclohexanone to produce value-added cyclohexanone oxime from under renewable electrocatalysis or, serve as zinc- $\text{NO}_2^-$  battery for energy storage.<sup>[31–33]</sup> These findings reliably eliminate hazards of  $\text{NO}_2^-$  to the environment strengthening rational significance of the electrooxidation of urea to  $\text{NO}_2^-$ . Thus, as the intention of UOR is to decrease energy depletion and costs for  $\text{H}_2$  production,<sup>[2,3]</sup> a practical tailoring of catalysts to direct electrooxidation urea to  $\text{NO}_2^-$  with boosted activity is attractive.

It is widely acknowledged that activity and selectivity of electrocatalysts is closely related to adsorption behavior of the intermediates on the catalyst surface.<sup>[34]</sup> Tuning catalyst electronic structure to regulate the adsorption behavior of intermediates can therefore be used to help optimize catalyst performance.<sup>[35–37]</sup> This has been widely reported for simple reactions including, HER and OER.<sup>[38]</sup> However, for UOR, because of multiple intermediates with complex electron/proton transfers, there are more to be considered, namely, the: 1) Intermediates for UOR are competitively adsorbed on the catalyst with the OER under high oxidation potential, which affects the UOR activity;<sup>[18,24]</sup> 2) Intermediates for UOR involve multiple atoms (carbon, oxygen, and nitrogen), which will be adsorbed on the catalyst through different atoms with a range of adsorption configurations for UOR pathways altering and selectivity changing.<sup>[16,22]</sup> Therefore to direct the reaction pathway and promote urea-to- $\text{NO}_2^-$  electrooxidation, intermediates adsorption tuning needs to be the focus in design of the catalyst.

Here we report that through doping Co and germanium (Ge) in  $\text{Ni}(\text{OH})_2$  (denoted as NiCoGe), the electronic structure of catalyst is tailored and tuned to direct adsorption behavior of the urea intermediates, with resulting boosted activity of urea to  $\text{NO}_2^-$  electrooxidation. We evidence that NiCoGe enables urea-to- $\text{NO}_2^-$  production with a significantly high selectivity of 84.9% Faradaic efficiency (FE) and boosted UOR activity of  $448.0 \text{ mA cm}^{-2}$  at 1.4 V versus reversible hydrogen electrode ( $V_{\text{RHE}}$ ). Importantly, we show this performance is better than reported NiCo catalysts and Ni-based catalysts. We confirm using judiciously combined in situ spectroscopy and density

functional theory (DFT) computation that co-doped Co and Ge optimize electronic structure of NiCoGe to regulate adsorbed urea from NN-terminal to NO-terminal configuration. In this way the C–N cleavage of urea to \*NH is facilitated, thus steering the urea-to- $\text{NO}_2^-$  pathway and boosting UOR.

## 2. Results and Discussion

### 2.1. Synthesis and UOR Performance of NiCoGe

NiCoGe catalyst was synthesized via a solvothermal method in which cleaned Ni foam (NF) was immersed with a mixture of hexamethylenetetramine,  $\text{Ni}(\text{NO}_3)_2 \cdot 6\text{H}_2\text{O}$ ,  $\text{Co}(\text{NO}_3)_2 \cdot 6\text{H}_2\text{O}$ ,  $\text{GeO}_2$  and water, and heated at  $120^\circ\text{C}$  for 10 h. Scanning electron microscope (SEM) and high-angle annular dark-field scanning transmission electron microscopy (HAADF-STEM) images evidenced that the morphology of as-synthesized product is a “wrinkled” nanosheet (NS) that can be readily assembled on the surface of NF (Figure 2a; Figures S1a–d, Supporting Information). Element mapping images confirmed that Ni, Co, and Ge are uniformly distributed on the NSs, evidencing that Co and Ge were co-doped successfully (Figure 2b). The ratios of Ni/Co/Ge in NS were determined to be 78.0/15.5/6.5 via scanning electron microscopy energy-dispersive X-ray spectroscopy (SEM-EDS) (Figure S1e, Supporting Information). Powder X-ray diffraction (XRD) confirmed that the diffraction peak for NiCoGe is similar to that for NiFe hydrotalcite, suggesting the phase structure for NiCoGe is layer double hydroxide (LDH, Figure S1f, Supporting Information).

NiCoGe grown on NF served as working electrodes to assess UOR. Given that concentration of urea in human urine is ca. 2 to 2.5 wt.% ( $\approx 0.33 \text{ M}$ ), 1 M KOH with 0.33 M urea solution was selected as electrolyte for testing. For comparison, Ni and NiCo hydroxide grown on NF (denoted as Ni and NiCo) with similar morphology, phase, and structure to NiCoGe, were synthesized (Figures S2 and S3, Supporting Information). Figure 2c presents the linear sweep voltammetry (LSV) curves for NiCoGe for OER and UOR. It is apparent that UOR exhibits an earlier onset potential than that for OER. To exhibit a current density of  $100 \text{ mA cm}^{-2}$ , the needed potential for UOR on

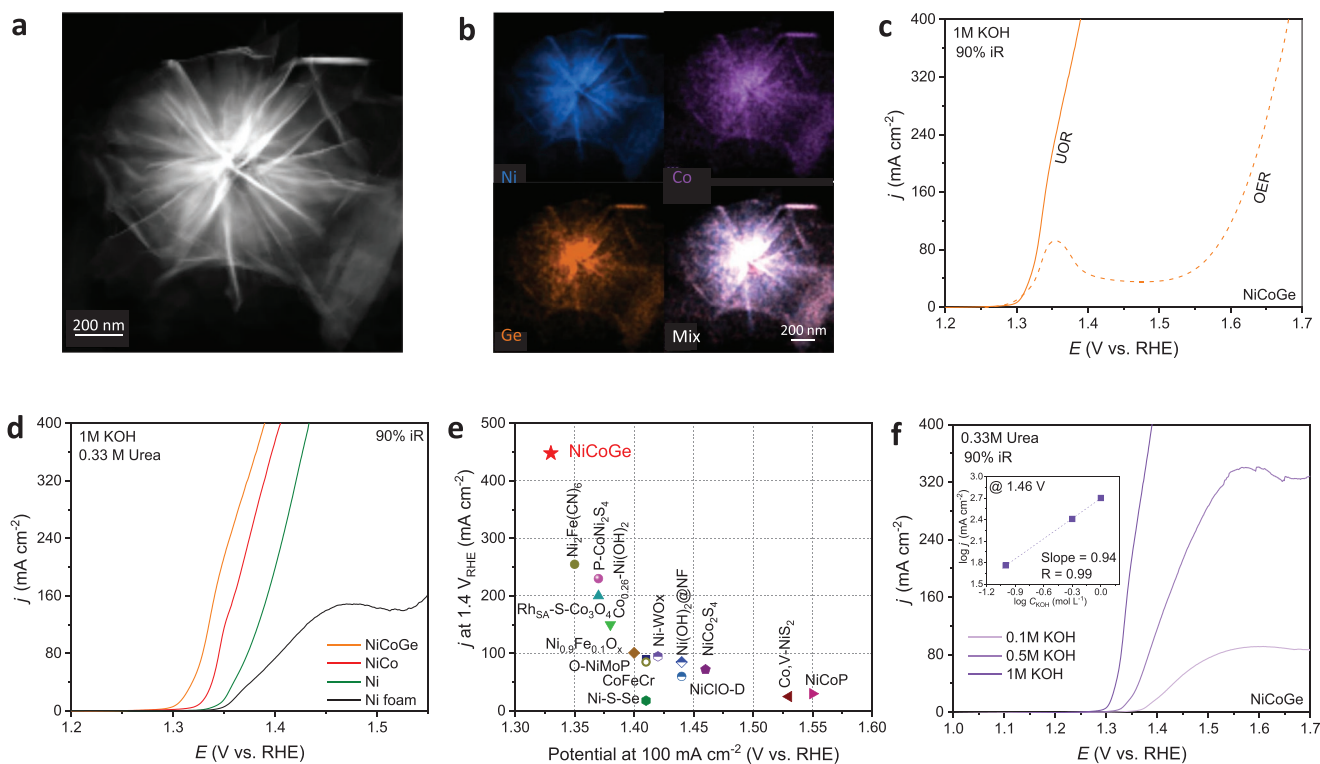


**Figure 2.** Morphology and UOR performance for NiCoGe catalyst. a) HAADF–STEM image and corresponding b) EDS elemental mapping image for NiCoGe. c) LSV curves for NiCoGe for UOR and OER. d) LSV curves for NiCoGe and compared catalysts in 1.0 m KOH containing 0.33 m urea. e) Comparison of UOR activity with reported Ni-based catalysts. f) LSV curves for NiCoGe for UOR under selected concentration of KOH electrolyte for UOR. Inset: Dependence of UOR current density on KOH concentration at 1.46  $V_{\text{RHE}}$ .

NiCoGe is 1.33  $V_{\text{RHE}}$  while it is 1.59  $V_{\text{RHE}}$  for OER, which gives a voltage difference  $> \approx 260$  mV. This finding confirms that NiCoGe is effective to drive UOR instead of OER for energy savings. Contrasting LSV curves for Ni, NiCo, and NiCoGe catalysts for UOR are presented as Figure 2d. The onset potential for UOR for these catalysts exhibits a decreased trend, namely, NiCoGe  $<$  NiCo  $<$  Ni, evidencing that UOR activity is significantly boosted with the Co and Ge doping. Importantly, NiCoGe exhibits “best” UOR with current density of 448.0  $\text{mA cm}^{-2}$  at 1.4  $V_{\text{RHE}}$ , a value significantly greater than that for NiCo and Ni of 375.8 and 199.3  $\text{mA cm}^{-2}$ , respectively (Figure S4, Supporting Information). This boosted activity for NiCoGe is greater than for reported Ni-based catalysts as is shown in Figure 2e and Table S1 (Supporting Information). Additional kinetic study evidenced that UOR for NiCoGe has an apparent dependence on the concentration of KOH, leading to a reaction order of 0.94 in relation to  $\text{OH}^-$  concentration (Figure 2f). The slope for pH with respect to onset potential was determined to be 89  $\text{mV pH}^{-1}$  (Figure S5, Supporting Information). Findings confirm the dependence of  $\text{OH}^-$  concentration on UOR for NiCoGe is Nernstian-type dependence, with rate determination step (RDS) as one electron–proton-coupled transfer. This  $\text{OH}^-$  dependent reaction order for NiCoGe is significantly different to that reported for urea-to- $\text{N}_2$  electrooxidation on NiOOH catalysts, because the RDS for the latter is  $\text{CO}_2$  desorption and needs two-electron transfer with two  $\text{OH}^-$  participation.<sup>[17,21]</sup> Because of the discrepancy in  $\text{OH}^-$  reaction order on NiCoGe (one) and that reported for NiOOH (two), it was concluded

therefore that electrooxidation urea to  $\text{N}_2$  is likely not the major process for NiCoGe, and that other reaction pathways might exist.

UOR products for NiCoGe were determined. In situ differential electrochemical mass spectrometry (DEMS) was carried out to determine potential dependent, gas production during UOR. As is shown in Figure 3a,b, with cyclic voltammetry (CV) scanning, the gas signal for  $\text{N}_2$  and oxygen ( $\text{O}_2$ ) that, originate respectively, from UOR and OER, were detected on the catalysts. The  $\text{N}_2$  signal is apparent at  $\approx 1.3 V_{\text{RHE}}$  for both NiCo and NiCoGe, and gradually increases to maximum at 1.7  $V_{\text{RHE}}$ . The  $\text{O}_2$  signal combined with the current decay for CV appeared at  $\approx 1.5 V_{\text{RHE}}$  for NiCo while it is later for NiCoGe at  $\approx 1.6 V_{\text{RHE}}$ . In particular, the ratio for  $\text{N}_2/\text{O}_2$  for NiCoGe at corresponding potentials is significantly greater than that for NiCo. These findings evidence that NiCoGe favors suppressing undesired OER for UOR, consistent with experimental findings from the rotating ring-disk electrode (RRDE) test (Figure S6, Supporting Information). Ion chromatography (IC) was used to analyze liquid products from UOR. A number of peaks appeared in NiCoGe samples following UOR at differing potential (Figure 3c). Via a comparing with the standard solution (Figure S7, Supporting Information), we confirmed that a mass of  $\text{NO}_2^-$  was generated for NiCoGe during UOR together with affiliated cyanate ( $\text{CNO}^-$ ), carbonate ( $\text{CO}_3^{2-}$ ) and a “small” amount of  $\text{NO}_3^-$ . Additionally, trace  $\text{NH}_4^+$  that was original from urea hydrolysis was detected in the solution via colorimetry (Figure S8, Supporting Information).

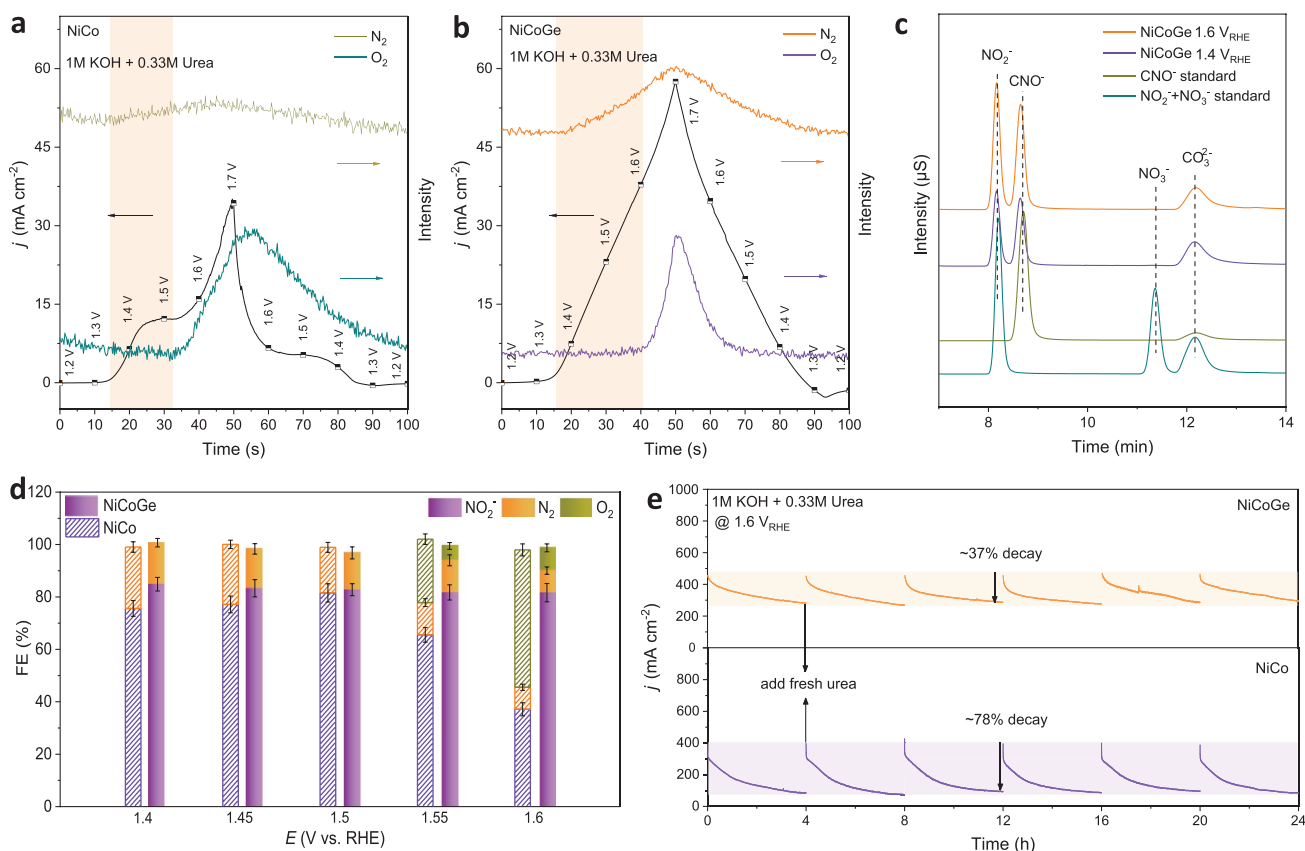


**Figure 3.** Products analysis for NiCoGe. In situ DEMS with corresponding CV curve for a) NiCo and b) NiCoGe, catalysts to *operando* monitor gases  $N_2$  and  $O_2$  during UOR, scan rate =  $10 \text{ mV s}^{-1}$ , no iR correction. c) IC curves for electrolytes following UOR catalyzed via NiCoGe at 1.4 and 1.6  $V_{\text{RHE}}$  for 1 h. IC curves for  $\text{NO}_2^-$ ,  $\text{NO}_3^-$ , and  $\text{CNO}^-$  standard. d) FEs for UOR products for NiCoGe under applied potential. e) Stability test for UOR for NiCo and NiCoGe under 1.6  $V_{\text{RHE}}$ , no iR correction.

The IC and gas chromatography (GC) determinations and potential dependency of FEs for each product were quantified and are summarized as Figure 3d.  $\text{NO}_2^-$  is the major N-containing product from NiCoGe UOR, together with  $N_2$ , trace  $\text{NO}_3^-$  and negligible  $N_2\text{O}$ . In addition, “minor”  $O_2$  is produced when potential is  $> 1.55 V_{\text{RHE}}$  (Figure S9, Supporting Information). Compared to the Ni, the FE for  $\text{NO}_2^-$  for NiCoGe are greater in each potential over 80% and reach a maximum of 84.9% at 1.4  $V_{\text{RHE}}$  (Figure 3d; Figure S10, Supporting Information). In contrast, the FE for  $\text{NO}_2^-$  for NiCo is significantly depressed to 37.1% at 1.6  $V_{\text{RHE}}$  because of OER competition, while that for NiCoGe is maintained as high as 81.6%. The partial current density for  $\text{NO}_2^-$  for NiCoGe reaches  $338.5 \text{ mA cm}^{-2}$  at 1.6  $V_{\text{RHE}}$ , which is 2.58 times greater than that for NiCo of  $131.0 \text{ mA cm}^{-2}$  (Figure S11, Supporting Information). Additionally, the electrochemically active surface area (ECSA) and mass loading normalized current density for UOR for these catalyst evidences that improved urea-to- $\text{NO}_2^-$  conversion for NiCoGe is intrinsic, and not related to ECSA and the mass loading of catalyst (Figures S12 and S13, Supporting Information). The UOR test under higher urea concentration of 2 M at 1.6  $V_{\text{RHE}}$  rules out the impact of OER on products selectivity where FE for  $\text{NO}_2^-$  for NiCoGe remains greater than that for NiCo. (Figure S14, Supporting Information). All these findings together confirm that urea-to- $\text{NO}_2^-$  is promoted on NiCoGe under Co, Ge co-doping, leading to boosted UOR.

The stability of NiCoGe was assessed via long-term chronopotentiometry testing at 1.6  $V_{\text{RHE}}$ . As is shown in Figure 3e, the UOR activity for NiCo and NiCoGe gradually decrease with 4 h large current operation. On refreshing the urea solution, the decayed activity of catalysts recovers meaningfully, even the initial stage for NiCoGe. Based on dependence of urea concentration on UOR (Figure S15, Supporting Information) the activity decay here is attributed to urea consumption, that is confirmed in the LSV curves for catalysts following UOR (Figure S16, Supporting Information). Despite more rapid urea consumption of NiCoGe during stability testing, the activity decay for NiCoGe at *ca.*  $\approx 37\%$  is significantly less than that for NiCo at *ca.*  $\approx 78\%$ , evidencing an increased stability of NiCoGe for UOR compared with NiCo. This result is attributed to the suppressed OER on NiCoGe under large current operation that prevents adverse evolution of Ni sites for activity loss. Importantly, in six consecutive UOR (24 h), the refreshed current density for NiCoGe did not apparently decay. SEM image, XRD, and EDS patterns for spent NiCoGe exhibit a morphology, phase and composition that are all but maintained following stability testing (Figure S17, Supporting Information). Additionally, the metal concentration determined following UOR evidenced that some metals leached into solution. Time-dependent findings confirmed that leaching initiates at the reaction beginning, i.e., within 1.5 h and ceases following. Importantly, compared with the initial



amount of NiCoGe, the total leached is negligible (Figure S18, Supporting Information). It is reliably concluded therefore that Co, Ge co-doping promotes urea-to- $\text{NO}_2^-$  electrooxidation and boosts activity and stability of NiCoGe for UOR.

## 2.2. Structural Characterization of NiCoGe under UOR

To determine the effect of Co, Ge co-doping on NiCoGe for directed urea-to- $\text{NO}_2^-$  electrooxidation, a series of structural characterization was conducted for NiCoGe during /or following UOR. In situ Raman spectra was performed to analyze dynamic structural evolution of catalysts during UOR. As is shown in Figure 4a,b, two peaks indexed to NiOOH are apparent for NiCo and NiCoGe with applied potential > 1.5  $V_{\text{RHE}}$ , demonstrating a structural transformation of Ni(OH)<sub>2</sub>

to NiOOH on the catalysts during UOR. The accumulation of NiOOH on NiCo is faster than that on NiCoGe because of the increased peak area. Importantly, compared with the NiOOH peaks for NiCo, they vanish for NiCoGe if the applied potential is changed from 1.7 to 1.3  $V_{\text{RHE}}$ . In combination with findings from reported studies with NiOOH for UOR,<sup>[8,24]</sup> the difference in Raman results here evidences that evolved NiOOH on NiCoGe is more active and accessible than that for NiCo, which rapidly reverses to initial Ni(OH)<sub>2</sub> through a spontaneous redox with urea. This finding confirms therefore that the Ge-doping reduces the significant valence increase on Ni sites, obviating NiOOH over-accumulation induced OER competition that boosts UOR kinetics.

The valence state change for NiCoGe and NiCo for UOR was characterized via X-ray absorption spectra (XAS). The X-ray absorption near-edge structure (XANES) spectra evidenced that

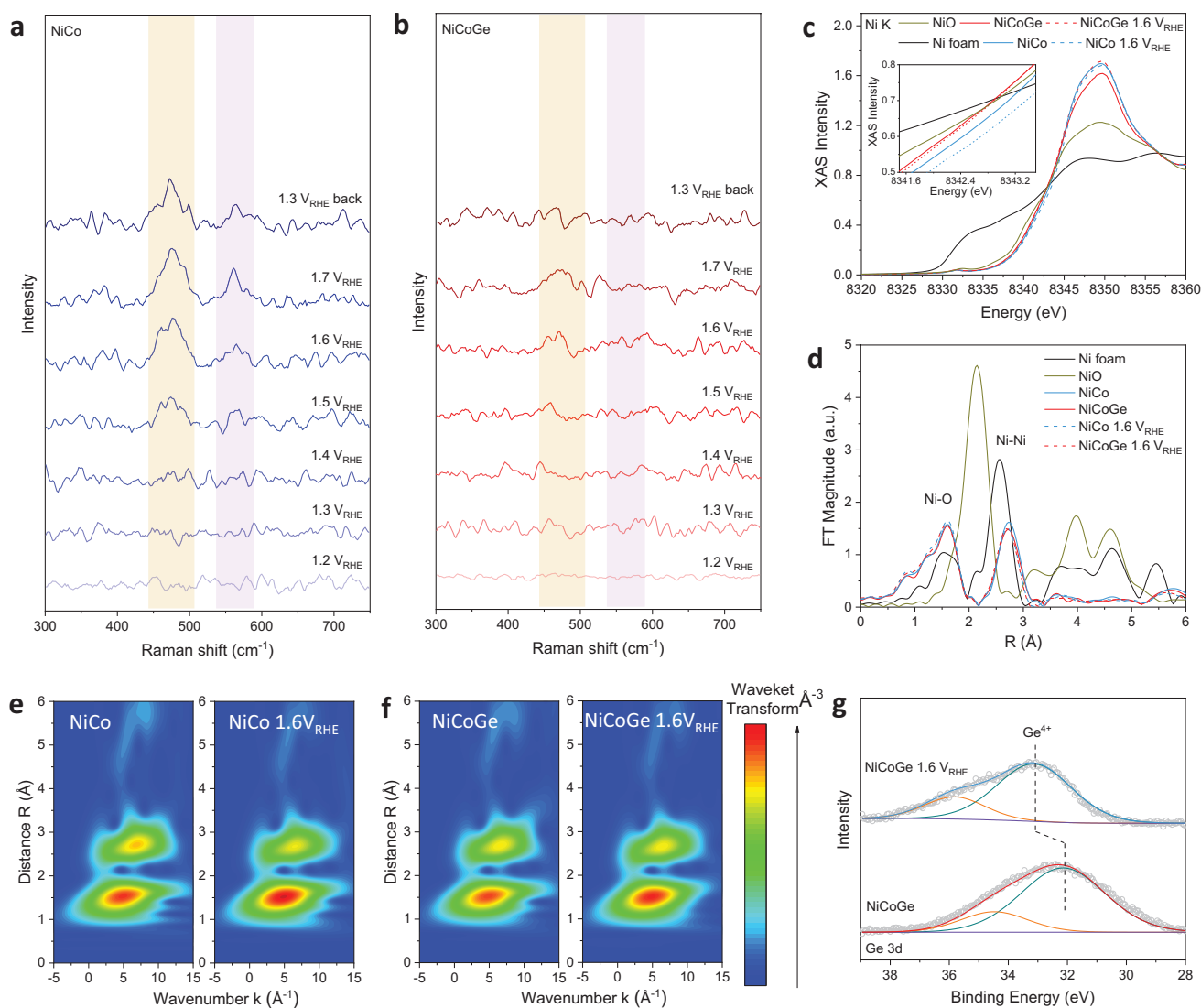


**Figure 4.** Structure characterizations for NiCoGe catalyst following UOR. In situ electrochemistry Raman spectra for UOR catalyzed by, a) NiCo and b) NiCoGe, at potential 1.20 to 1.70  $V_{\text{RHE}}$  and back to 1.3  $V_{\text{RHE}}$ . c) XANES, and d) EXAFS spectra and e, f) Wavelet transform image for EXAFS data with optimized Morlet parameter ( $\kappa = 5$ ,  $\sigma = 1$ ) at Ni K-edge for e) NiCo and f) NiCoGe catalysts prior to and following UOR testing at 1.60  $V_{\text{RHE}}$ . g) Ge 3d XPS spectra for NiCoGe catalyst prior to and following UOR testing at 1.60  $V_{\text{RHE}}$ .

the position of Ni K-edge remains steady for NiCoGe during UOR, while it shifts to high energy for NiCo following UOR at 1.6  $V_{\text{RHE}}$  (Figure 4c; Figure S19, Supporting Information). This finding confirms that the valence state for Ni in NiCoGe is not increased with UOR potential.

In contrast an apparent valence state increase for Co is observed with both NiCo and NiCoGe as is confirmed by Co 3d X-ray photoelectron spectroscopy (XPS) and Co K-edge XANES (Figures S20 and S21, Supporting Information), evidencing the O atoms will preferentially coordinate with Co instead of Ni during UOR. The Ni K-edge extended X-ray absorption fine structure (EXAFS) spectra and fitted results demonstrate that the coordination number for Ni–O and Ni–Ni for as-prepared NiCo is, respectively, 6.50 and 7.00, while it changes to 6.83 and 6.88 following UOR at 1.6  $V_{\text{RHE}}$  (Figure 4d; Figure S22 and Table S2, Supporting Information). This is direct evidence for irreversible oxidation of  $\text{Ni}^{2+}$  to  $\text{Ni}^{3+}$  species in NiCo during UOR that is consistent with Raman and XPS findings (Figure S23, Supporting Information). However, compared to NiCo, negligible change is observed in the Ni K-edge EXAFS spectra for NiCoGe following UOR at 1.6  $V_{\text{RHE}}$ , even in the wavelet transform–EXAFS (WT–EXAFS, Figure 4e,f). Additionally, the Ge 3d XPS for NiCoGe evidences that the binding energy for Ge 3d peak shifts to a high level following UOR (Figure 4g). Taken together, it can be concluded from these findings that, 1) doped Co regulates the lattice oxygen ligand environment of evolved NiOOH via saturation of Co–O bonds during UOR and 2) doped Ge donates electrons to Ni sites during electrooxidation, resulting in an altered electronic structure for NiCoGe.

Because of the positive effect of Co, Ge dopants, the impact of amount of Ge, Co on UOR performance was determined. As seen in Figure S24 (Supporting Information), as Co doping increased in NiCo, from NiCo-1 to NiCo-3, the onset potential for UOR gradually reduced, while UOR activity at high potential was decreased. This finding, importantly, is consistent with those reported for NiCo for UOR. If more Ge is doped from NiCoGe-1 to NiCoGe-3, UOR performance is decreased. All these findings combined confirm that the amount of doping with Ge, Co is important to UOR performance. For Co,  $\approx 15.5\%$  atomic doping regulates and nominally optimizes the oxygen ligand environment for Ni sites and assists Ni self-oxidation to NiOOH under low potential leading to a lower onset potential for UOR. Low Ge doping with 6.5% changes electron structure of Ni sites via donating electrons during UOR that reduces the significant valence increase on Ni sites and, prevents over accumulation of NiOOH for activity decay under high potential.

### 2.3. Mechanistic Studies of NiCoGe for UOR

DFT computation was carried out to understand the mechanism of Co, Ge co-doping boosted urea-to- $\text{NO}_2^-$  electrooxidation. In the simulation the solvation effect using an implicit solvent model was considered (see Computational Methods in Supporting Information). Corresponding models for catalysts to match the experimental results were constructed. For NiCo a  $\beta$ -NiOOH (010) surface with  $2 \times 4 \times 4$  supercell in which one of the Ni atoms was replaced by Co was constructed. (Figures S25 and S26a, Supporting Information) The NiCoGe model was

similar with that for NiCo but an additional Ni atom was replaced by Ge (Figure S26b, Supporting Information). The adsorption behaviors for urea on NiCo and NiCoGe surface were determined. All possible, adsorption sites and configurations on NiCo and NiCoGe catalysts were considered under potential of zero charge (PZC), that is, the charge-neutral method (cnm, Tables S3 and S4, Supporting Information). Two “relatively” stable adsorption configurations were screened, including NN-terminal and O-/NO-terminal adsorptions on NiCo and NiCoGe surface (Figure 5a). It was found that urea tends to adsorb on NiCo and NiCoGe catalysts as O- and NN-terminals with corresponding adsorption energy of, respectively,  $-2.34$  and  $-3.45$  eV (Figure 5b), confirming that the doped Ge is able to modulate the adsorption behavior of NiCo on urea molecules. Significantly, the stable adsorption configuration of urea on NiCo and NiCoGe can be reversed when the applied potential of 1.5  $V_{\text{RHE}}$  is considered. As a result, the NN-terminal and NO-terminal adsorptions with the lowest adsorption energy of, respectively,  $-1.5$  and  $-0.94$  eV became apparently optimized adsorption configurations for NiCo and NiCoGe, underscoring the importance of surface charge in heterogeneous electrochemistry.<sup>[39]</sup>

In situ surface enhanced, attenuated total reflectance infrared absorption spectroscopy (ATR-SEIRAS) at different UOR potential, was carried out to determine the adsorbed intermediates and to identify the altered urea adsorption configuration for NiCoGe. To get better observation, a reference spectrum determined at 1.2  $V_{\text{RHE}}$  in 1 M KOH with 0.33 M urea was subtracted in the data findings. As is shown in Figure 5c,d, the ATR-SEIRAS for these catalysts exhibit new peaks that are assigned to the related intermediates for UOR based on reported findings (Table S5, Supporting Information).<sup>[22,40–42]</sup> Significantly, a C–N stretching vibration peak at  $\approx 1410$   $\text{cm}^{-1}$  for urea adsorbates on NiCo and NiCoGe and which is increased with applied potential.<sup>[22,40]</sup> However, the peak for C=O at  $\approx 1742$   $\text{cm}^{-1}$  that is evidence for NO-terminal adsorption only found in NiCoGe and not NiCo when the potential is  $> 1.4 V_{\text{RHE}}$ .<sup>[22]</sup> The variation in these peaks evidences that the configuration of urea adsorbates on NiCo and NiCoGe are different, something confirmed in the DFT findings. Therefore, the adsorbed urea on NiCo maintains as NN-terminal adsorption configuration, while it reverses to NO-terminal adsorption configuration on NiCoGe with UOR potential increase. It is reported that the reaction pathway for urea-to- $\text{NO}_2^-$  electrooxidation is significantly dependent on C–N cleavage.<sup>[7]</sup> Given this the UOR energetics for the C–N cleavage pathway with different local configurations of urea adsorbates on NiCo and NiCoGe were correlated. As can be seen in Figure 5e, the urea molecule first undergoes a dehydrogenation reaction to form  $^*\text{NHCONH}_2$  on NiCo and NiCoGe catalyst under an applied potential of 1.5  $V_{\text{RHE}}$ , corresponding to an energy, respectively, of 0.84 and 0.09 eV. A single peak located at  $\approx 3425$   $\text{cm}^{-1}$  was experimentally observed on the NiCoGe catalyst in the ATR-SEIRAS peak, which evidences the presence of  $^*\text{NH}$  as a key intermediate. However, for NiCo, the OH adsorption peak located at  $\approx 3232$   $\text{cm}^{-1}$  is increased instead of  $^*\text{NH}$ , Figure 5c,d. These findings confirm that compared with NiCo, the facilitated C–N cleavage on NiCoGe promotes  $^*\text{NH}$  adsorption and results in a high  $^*\text{NH}$  coverage to repel  $\text{OH}^-$ , thereby suppressing OER during

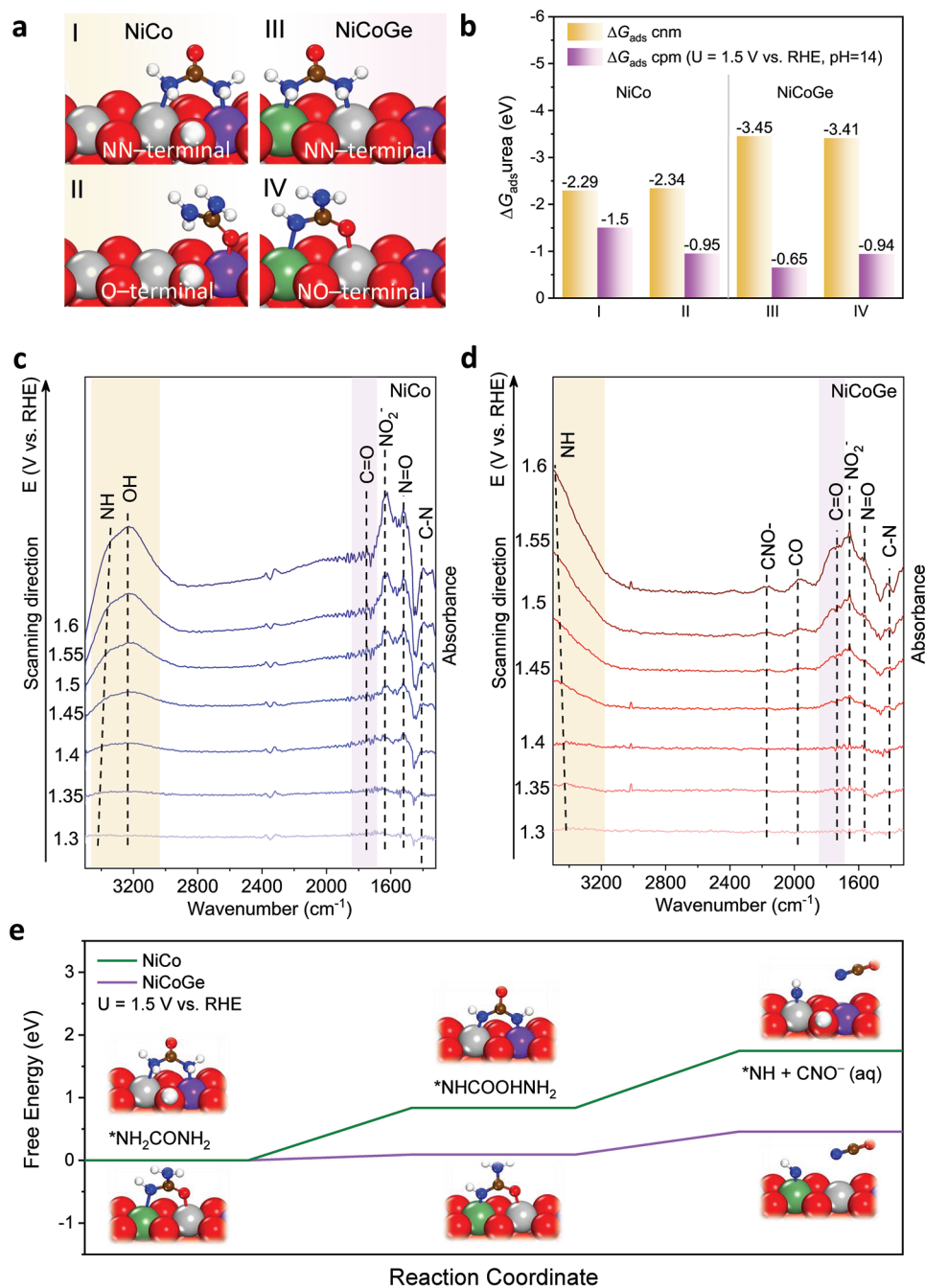


**Figure 5.** Adsorption behavior of UOR intermediates on NiCo and NiCoGe. a) Stable structures for urea molecules adsorbed on NiCo and NiCoGe catalysts. There are two corresponding configurations for NN-terminal and O/NO-terminal adsorptions. b) Adsorption energy for urea molecule in Figure 5a is based on charge-neutral and constant potential methods (cm and cpm). In situ ATR-SEIRAS was obtained during chronopotentiometry in a potential window 1.3 to 1.6  $V_{\text{RHE}}$  for, c) NiCo and d) NiCoGe under UOR. e) Free energy diagram for  $^*\text{NH}_2\text{CONH}_2$  oxidation to  $^*\text{NH} + \text{CNO}^- (\text{aq})$ . Light grey-color, purple, green, brown, red, white, and blue spheres represent, respectively, Ni, Co, Ge, C, O, H, and N atoms.

UOR. Additionally,  $\text{CNO}^-$  species was experimentally observed on NiCoGe catalyst with a wavenumber near  $2200 \text{ cm}^{-1}$ , while NiCo was absent. Based on these experimental findings, this is achieved theoretically via the reaction mechanism<sup>[6]</sup> namely,  $^*\text{NHCONH}_2 + 2\text{OH}^- \rightarrow ^*\text{NH} + 2\text{H}_2\text{O}(\text{l}) + \text{CNO}^- (\text{aq}) + \text{e}^-$ . Computed results evidence that formation of  $^*\text{NH}$  and  $\text{CNO}^-$  released into the bulk of the solution needs to overcome a free

energy barrier of, respectively, 0.91 and 0.37 eV for NiCo and NiCoGe catalyst. It is concluded therefore DFT data support that NiCoGe catalyst is more favourable for C–N bond cleavage than the NiCo catalyst.

Following cleavage of the C–N bond the dissociative  $^*\text{NH}$  will be absorbed on the surface of catalyst and the absorbed  $^*\text{NH}$  is continuously oxidized in the reaction step following.

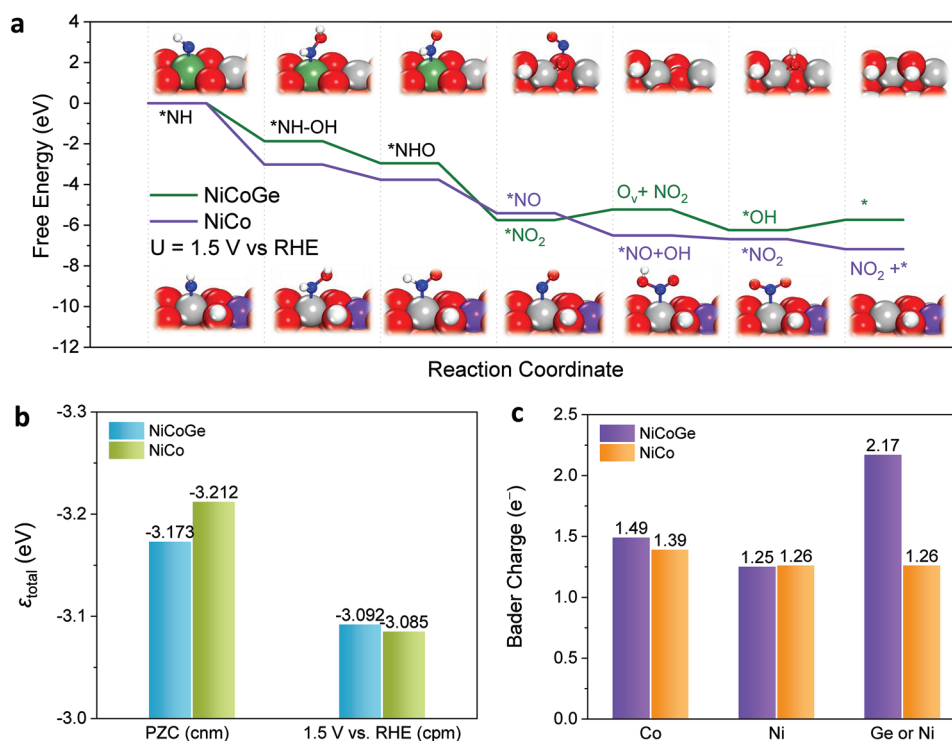


**Figure 6.** DFT simulation and mechanism for UOR to  $\text{NO}_2^-$  on NiCo and NiCoGe. a) Free energy diagram for  $^*\text{NH}$  oxidation to  $\text{NO}_2^-$  under applied potential  $1.5 V_{\text{RHE}}$ . b) Total band centre for NiCo and NiCoGe based on charge-neutral and constant-potential methods (cnm and cpm). c) Analyses for Bader charge of adjacent Co, Ni, and Ge/Ni at the first layer at  $U = 1.5 V_{\text{RHE}}$ . Light grey-color, purple, green, brown, red, white, and blue spheres represent, respectively, Ni, Co, Ge, C, O, H, and N atoms.

The free energy diagram for  $^*\text{NH}$  oxidation on NiCo and NiCoGe together with the structures for reaction intermediates were computed and are presented as **Figure 6a**. For the first three steps, the intermediates are the same for both catalysts. From the fourth step, the active site for the NiCo catalyst remains on the Ni atom, but the active site for NiCoGe become the O atom on the surface. Because NO adsorption on the Ge site is optimized as the initial structure the NO is adsorbed on the adjacent O atom following optimization, indicating a weaker adsorption of urea on the Ge site. For NiCo,  $^*\text{NO}$  undergoes a sequential two step oxidation reaction to form  $^*\text{NO}_2$  and then desorbed from the surface. However, the  $^*\text{NO}$  on NiCoGe combines with an O atom on the surface to form  $\text{NO}_2$  and then desorbs from the surface leaving an O vacancy. Following this the  $\text{OH}^-$  in solution occupies the vacancy and undergoes a further oxidation to form  $\text{H}_2\text{O}$  to return to a clean surface and, proceed to the next cycle. Combined with C–N cleavage, the potential determining steps for both NiCo and NiCoGe catalysts are  $^*\text{NHCONH}_2 + 2\text{OH}^- \rightarrow ^*\text{NH} + 2\text{H}_2\text{O} (\text{l}) + \text{CNO}^- (\text{aq}) + e^-$ , corresponding to free energy changes of, respectively, 0.91 and 0.37 eV. Therefore, the doping of Ge atom significantly promotes formation of  $\text{NO}_2^-$ , and is consistent with experimental findings that NiCoGe boosts UOR activity and selectivity for  $\text{NO}_2^-$  generation.

The doping with Ge that boosts catalytic performance of the pristine NiCo is attributed to the change in electronic properties. In general, the closer the centre of the band is to the Fermi level, the stronger the adsorption of intermediates.<sup>[43,44]</sup> As is shown in the total band centre of Figure 6b, the  $\epsilon_{\text{total}}$  value for

NiCoGe is closer to the Fermi level than NiCo, based on the charge-neutral method. For the constant potential method, there is an inversion where the  $\epsilon_{\text{total}}$  value for NiCo is closer to the Fermi level than NiCoGe. This explains the transformation of the adsorption behavior for urea molecules on the both catalysts. The adsorption behavior for  $^*\text{NO}$  on NiCoGe is different to NiCo because the Ge atom loses more electrons (donates the electrons to Ni as is evidenced via experimental), Figure 6c, and has not enough electrons to transfer to  $^*\text{NO}$  species, so that,  $^*\text{NO}$  adsorbs weakly at the Ge site and migrates to the adjacent O atom changing the pre-existing reaction pathway on NiCo catalyst under an applied potential of  $1.5 V_{\text{RHE}}$ .

### 3. Conclusion

We conclude that by co-doping Co, Ge in  $\text{Ni}(\text{OH})_2$ , the adsorption behavior of urea on the catalysts surface is directed for electrooxidation to  $\text{NO}_2^-$  products. The NiCoGe exhibits a FE of 84.9% for  $\text{NO}_2^-$  generation together with a boosted UOR activity of  $448.0 \text{ mA cm}^{-2}$  at  $1.4 V_{\text{RHE}}$ . This, importantly, is amongst best reported UOR activity for Ni-based catalysts. Combined in situ spectra and DFT computation confirm that boosted urea-to- $\text{NO}_2^-$  is directed via altered adsorption configurations of urea intermediates on the catalyst surface that significantly reduce the energy barrier for C–N cleavage for  $^*\text{NH}$  formation, and thereby, expedite the pathway for urea to  $\text{NO}_2^-$ . Our findings highlight the practical advantage of tuning of intermediates adsorption on directing the reaction pathway, and will be



of interest to researchers and manufacturers for design and boosted performance for a range of electrocatalytic reactions containing multiple intermediates.

## 4. Experimental Section

**Chemicals:** Nickel nitrate hexahydrate ( $\text{Ni}(\text{NO}_3)_2 \cdot 6\text{H}_2\text{O}$ , AR), Cobalt nitrate hexahydrate ( $\text{Co}(\text{NO}_3)_2 \cdot 6\text{H}_2\text{O}$ , AR), germanium dioxide ( $\text{GeO}_2$ , AR), potassium hydroxide (KOH, AR), and hexamethylenetetramine (HMA, AR) were purchased from Sigma–Aldrich. Argon (Ar, 99.999%) was purchased from BOC Gas (Australia). All chemicals were used as received without further modification. The water ( $18 \text{ M}\Omega \cdot \text{cm}$ ) used in experiments was prepared via passing through an ultra-pure purification system. NF ( $\approx 2.5 \times 2 \text{ cm}$ ) was carefully cleaned with 6 M HCl solution under ultrasonic condition for 30 min to remove the surface NiO layer, and acetone and ethanol were separately then used for 10 min to ensure the surface of nickel foam was cleaned. It was aired naturally.

**Preparation of NiCoGe Catalyst:** In a typical preparation of NiCoGe, grown NF, 72.7 mg  $\text{Ni}(\text{NO}_3)_2 \cdot 6\text{H}_2\text{O}$ , 14.6 mg  $\text{Co}(\text{NO}_3)_2 \cdot 6\text{H}_2\text{O}$ , 3 mg  $\text{GeO}_2$ , 210 mg HMA and 10 mL water were added into a 30 mL vial and ultrasonicated for ca. 0.5 h to produce a homogeneous solution. The concentration for each precursor  $\text{Ni}(\text{NO}_3)_2 \cdot 6\text{H}_2\text{O}$ ,  $\text{Co}(\text{NO}_3)_2 \cdot 6\text{H}_2\text{O}$  and  $\text{GeO}_2$  were, respectively, 25.1, 50.2, and 2.87 mM. This resulting mixture with a selected piece of NF was transferred to a 30 mL Teflon-lined stainless-steel autoclave and heated at 150 °C for 10 h before cooling to room temperature (RT) (ca. 25 °C) naturally. A dark green-color, thin film on the metal substrate was formed that was rinsed with 10 mL distilled water, followed by 10 mL ethanol with ultrasonication for 5 min, and dried at 60 °C for 2 h in an air-oven. The preparation of NiCo and Ni was similar to that for NiCoGe except for removing corresponding metal precursors. The mass loading for catalyst on NF were determined via subtracting the mass of NFs prior to and following synthesis (Table S6, Supporting Information) and were, respectively, 1.4, 1.6, and 1.7 mg for Ni, NiCo, and NiCoGe.

**Characterizations:** The aberration-corrected transmission electron microscope images, high-angle annular dark-field imaging, and EDS mapping were taken on a FEI Titan Themis 80–200 operating at 200 kV. The samples were prepared via dropping ethanol dispersion of samples onto carbon-coated copper TEM grids using pipettes, and dried at RT. XRD data were determined on a Rigaku MiniFlex 600 X-Ray Diffractometer. XPS was carried out under ultra-high vacuum on a Kratos Axis Ultra with a Delay Line Detector photoelectron spectrometer using an Al monochromatic X-ray source. The carbon peak at 284.6 eV was used as a reference to correct for charging effect(s). Ultraviolet-visible (UV-vis) spectra were determined on SHIMADZU UV-2600 spectrophotometer. Synchrotron-based XAS data were determined at the XAS beamline of the Australian Synchrotron. Data were processed using standard procedures using the Demeter program package (Version 0.9.24).

**Electrochemical Measurements:** Electrochemical oxidation of urea was conducted in a gas-tight H-cell separated by a proton exchange membrane (Nafion 117). A micro Ag/AgCl electrode (4.0 M KCl) and graphite rod were used as, respectively, reference and counter, electrode. Catalyst-grown Ni foam was used as working electrode (active area:  $0.5 \times 0.5 \text{ cm}$ ,  $0.25 \text{ cm}^2$ ). The electrolyte was 1.0 M KOH with a 0.33 M urea solution. Each compartment contained 15 mL electrolyte with ca. 20 mL headspace. Ar was delivered to the anodic compartment (connected directly to GC (Agilent 8890B)) at a constant rate of 20 sccm and allowed to purge for 30 min prior to experiment. The reaction was tested on CHI760e electrochemical workstation by LSV with scan rate of  $5 \text{ mV s}^{-1}$  or, chronoamperometry under selected potential. Gaseous products were analyzed via GC equipped with a PLOT MolSieve 5A column and a Q-bond PLOT column. Liquid products were characterized via IC (Thermo Scientific Dionex Integriion RFI) with a Dionex IonPac AS19–4um  $2 \times 250 \text{ mm}$  column. Potentials were given against RHE computed from the Nernst equation. Related readouts were recorded

with 90% ohmic iR drop correction. The FE of reaction products was computed from:  $\text{FE} = eF \times n/Q = eF \times n/(I \times t)$ , where  $e$  is the number of electrons transferred,  $F$  Faraday constant,  $Q$  charge,  $I$  current,  $t$  running time and  $n$  total of product (mole).

## Supporting Information

Supporting Information is available from the Wiley Online Library or from the author.

## Acknowledgements

P.W. and X.B. contributed equally to this work. This work was financially supported by the Australian Research Council (ARC) through Discovery and Linkage Projects Program (FL170100154, DP220102596, LP210301397). XAS testing was undertaken on the XAS beamline at the Australian Synchrotron, part of ANSTO.

Open access publishing facilitated by The University of Adelaide, as part of the Wiley - The University of Adelaide agreement via the Council of Australian University Librarians.

## Conflict of Interest

The authors declare no conflict of interest.

## Data Availability Statement

The data that support the findings of this study are available from the corresponding author upon reasonable request.

## Keywords

adsorption tuning, electrocatalysts, nitrite, urea oxidation reaction

Received: February 17, 2023  
Published online: March 16, 2023

- [1] A. N. Rollinson, J. Jones, V. Dupont, M. V. Twigg, *Energy Environ. Sci.* **2011**, 4, 1216.
- [2] B. K. Boggs, R. L. King, G. G. Botte, *Chem. Commun.* **2009**, 32, 4859.
- [3] X. Sun, R. Ding, *Catal. Sci. Technol.* **2020**, 10, 1567.
- [4] J.-Y. Zhang, T. He, M. Wang, R. Qi, Y. Yan, Z. Dong, H. Liu, H. Wang, B. Y. Xia, *Nano Energy* **2019**, 60, 894.
- [5] H. Jiang, M. Sun, S. Wu, B. Huang, C.-S. Lee, W. Zhang, *Adv. Funct. Mater.* **2021**, 31, 2104951.
- [6] S. W. Tatarchuk, J. J. Medvedev, F. Li, Y. Tobolovskaya, A. Klinkova, *Angew. Chem., Int. Ed.* **2022**, 61, 202209839.
- [7] J. Li, J. Li, T. Liu, L. Chen, Y. Li, H. Wang, X. Chen, M. Gong, Z. P. Liu, X. Yang, *Angew. Chem., Int. Ed.* **2021**, 60, 26656.
- [8] W. Chen, L. Xu, X. Zhu, Y.-C. Huang, W. Zhou, D. Wang, Y. Zhou, S. Du, Q. Li, C. Xie, L. Tao, C.-L. Dong, J. Liu, Y. Wang, R. Chen, H. Su, C. Chen, Y. Zou, Y. Li, Q. Liu, S. Wang, *Angew. Chem., Int. Ed.* **2021**, 60, 7297.
- [9] X. Hu, J. Zhu, J. Li, Q. Wu, *ChemElectroChem* **2020**, 7, 3211.
- [10] L. Zhang, L. Wang, H. Lin, Y. Liu, J. Ye, Y. Wen, A. Chen, L. Wang, F. Ni, Z. Zhou, S. Sun, Y. Li, B. Zhang, H. Peng, *Angew. Chem., Int. Ed.* **2019**, 58, 16820.

- [11] R. P. Forslund, J. T. Mefford, W. G. Hardin, C. T. Alexander, K. P. Johnston, K. J. Stevenson, *ACS Catal.* **2016**, *6*, 5044.
- [12] Z. Ji, Y. Song, S. Zhao, Y. Li, J. Liu, W. Hu, *ACS Catal.* **2022**, *12*, 569.
- [13] Q. Zhang, F. M. D. Kazim, S. Ma, K. Qu, M. Li, Y. Wang, H. Hu, W. Cai, Z. Yang, *Appl. Catal., B* **2021**, *280*, 119436.
- [14] X. F. Lu, S. L. Zhang, W. L. Sim, S. Gao, X. W. Lou, *Angew. Chem., Int. Ed.* **2021**, *60*, 22885.
- [15] C. Li, Y. Liu, Z. Zhuo, H. Ju, D. Li, Y. Guo, X. Wu, H. Li, T. Zhai, *Adv. Energy Mater.* **2018**, *8*, 1801775.
- [16] W.-K. Han, J.-X. Wei, K. Xiao, T. Ouyang, X. Peng, S. Zhao, Z.-Q. Liu, *Angew. Chem., Int. Ed.* **2022**, *61*, 202206050.
- [17] S.-K. Geng, Y. Zheng, S.-Q. Li, H. Su, X. Zhao, J. Hu, H.-B. Shu, M. Jaroniec, P. Chen, Q.-H. Liu, S.-Z. Qiao, *Nat. Energy* **2021**, *6*, 904.
- [18] M. Zeng, J. Wu, Z. Li, H. Wu, J. Wang, H. Wang, L. He, X. Yang, *ACS Sustainable Chem. Eng.* **2019**, *7*, 4777.
- [19] A. Nadeema, V. Kashyap, R. Gururaj, S. Kurungot, *ACS Appl. Mater. Interfaces* **2019**, *11*, 25917.
- [20] Z.-Y. Yu, C.-C. Lang, M.-R. Gao, Y. Chen, Q.-Q. Fu, Y. Duan, S.-H. Yu, *Energy Environ. Sci.* **2018**, *11*, 1890.
- [21] D. Liu, T. Liu, L. Zhang, F. Qu, G. Du, A. M. Asiri, X. Sun, *J. Mater. Chem. A* **2017**, *5*, 3208.
- [22] D. A. Daramola, D. Singh, G. G. Botte, *J. Phys. Chem. A* **2010**, *114*, 11513.
- [23] X. Wang, J.-P. Li, Y. Duan, J. Li, H. Wang, X. Yang, M. Gong, *ChemCatChem* **2022**, *14*, 202101906.
- [24] R. Lin, L. Kang, T. Zhao, J. Feng, V. Celorrio, G. Zhang, G. Cibin, A. Kucernak, D. J. L. Brett, F. Corà, I. P. Parkin, G. He, *Energy Environ. Sci.* **2022**, *15*, 2386.
- [25] D. Zhu, H. Zhang, J. Miao, F. Hu, L. Wang, Y. Tang, M. Qiao, C. Guo, *J. Mater. Chem. A* **2022**, *10*, 3296.
- [26] V. Vedharathinam, G. G. Botte, *Electrochim. Acta* **2012**, *81*, 292.
- [27] L. Wang, Y. Zhu, Y. Wen, S. Li, C. Cui, F. Ni, Y. Liu, H. Lin, Y. Li, H. Peng, B. Zhang, *Angew. Chem., Int. Ed.* **2021**, *60*, 10577.
- [28] F.-Y. Chen, Z.-Y. Wu, S. Gupta, D. J. Rivera, S. V. Lambeets, S. Pecaut, J. Y. T. Kim, P. Zhu, Y. Z. Finrock, D. M. Meira, G. King, G. Gao, W. Xu, D. A. Cullen, H. Zhou, Y. Han, D. E. Perea, C. L. Muhich, H. Wang, *Nat. Nanotechnol.* **2022**, *17*, 759.
- [29] J. Liang, Q. Liu, A. A. Alshehri, X. Sun, *Nano Res. Energy* **2022**, *1*, 9120010.
- [30] J. Liang, L. Zhang, X. He, Y. Wang, Y. Luo, D. Zheng, S. Sun, Z. Cai, J. Zhang, K. Ma, Y. Zheng, X. Sun, C. Tang, *J. Mater. Chem. A* **2023**, *11*, 1098.
- [31] X. Zhang, H. Jing, S. Chen, B. Liu, L. Yu, J. Xiao, D. Deng, *Chem Catal.* **2022**, *2*, 1807.
- [32] Y. Guo, R. Zhang, S. Zhang, Y. Zhao, Q. Yang, Z. Huang, B. Dong, C. Zhi, *Energy Environ. Sci.* **2021**, *14*, 3938.
- [33] R. Zhang, Y. Guo, S. Zhang, D. Chen, Y. Zhao, Z. Huang, L. Ma, P. Li, Q. Yang, G. Liang, C. Zhi, *Adv. Energy Mater.* **2022**, *12*, 2103872.
- [34] J. K. Nørskov, F. Studt, F. Abild-Pedersen, T. Bligaard, *Fundamental Concepts in Heterogeneous Catalysis*, John Wiley & Sons, New York **2014**.
- [35] P. Wang, H. Yang, C. Tang, Y. Wu, Y. Zheng, T. Cheng, K. Davey, X. Huang, S. Z. Qiao, *Nat. Commun.* **2022**, *13*, 3754.
- [36] Y. Ji, Z. Chen, R. Wei, C. Yang, Y. Wang, J. Xu, H. Zhang, A. Guan, J. Chen, T.-K. Sham, J. Luo, Y. Yang, X. Xu, G. Zheng, *Nat. Catal.* **2022**, *5*, 251.
- [37] X. Wang, Y. Jiao, L. Li, Y. Zheng, S. Z. Qiao, *Angew. Chem., Int. Ed.* **2022**, *61*, 202114253.
- [38] Y. Jiao, Y. Zheng, M. Jaroniec, S. Z. Qiao, *Chem. Soc. Rev.* **2015**, *44*, 2060.
- [39] X. Zhao, Z. H. Levell, S. Yu, Y. Liu, *Chem. Rev.* **2022**, *122*, 10675.
- [40] A. C. S. Bezerra, E. L. de Sá, F. C. Nart, *J. Phys. Chem. B* **1997**, *101*, 6443.
- [41] O. Yépez, B. R. Scharifker, *Electrochim. Acta* **2005**, *50*, 1423.
- [42] R. Gómez, A. Rodes, J. M. Orts, J. M. Feliu, J. M. Pérez, *Surf. Sci.* **1995**, *342*, L1104.
- [43] J. K. Nørskov, F. Abild-Pedersen, F. Studt, T. Bligaard, *Proc. Natl. Acad. Sci. USA* **2011**, *108*, 937.
- [44] B. Hammer, J. K. Nørskov, *Nature* **1995**, *376*, 238.